Energetic electron precipitation during high-speed solar wind stream driven storms

Nigel P. Meredith,[1] Richard B. Horne,[1] Mai Mai Lam,[2] Michael H. Denton,[3] Joseph E. Borovsky,[4] and Janet C. Green[5]

Received 16 November 2010; revised 25 February 2011; accepted 9 March 2011; published 28 May 2011.

[1] Electron precipitation from the Earth's inner magnetosphere transmits solar variability to the Earth's upper atmosphere and may affect surface level climate. Here we conduct a superposed epoch analysis of energetic electrons observed by the NOAA POES spacecraft during 42 high-speed solar wind stream (HSS) driven geomagnetic storms to determine the temporal evolution and global distribution of the precipitating flux. The flux of trapped and precipitating $E > 30$ keV electrons increases immediately following storm onset and remains elevated during the passage of the HSS. In contrast, the trapped and precipitating relativistic electrons (E > 1 MeV) drop out following storm onset and subsequently increase during the recovery phase to levels which eventually exceed the prestorm levels. There is no evidence for enhanced precipitation of relativistic electrons during the MeV flux drop out, suggesting that flux drop outs during the main phase of HSS-driven storms are not due to precipitation to the atmosphere. On average, the flux of precipitating $E > 30$ keV electrons is enhanced by a factor of ~10 during the passage of the high-speed stream at all geographic longitudes. In contrast, the precipitating relativistic electron count rate is observed to peak in the region poleward of the South Atlantic Anomaly. During the passage of the high-speed stream, the flux of precipitating $E > 30$ keV electrons peaks in the region from 2100 to 1200 magnetic local time at low L ($4 < L < 7$) and in the prenoon sector at high L ($7 < L < 9$), suggesting that chorus waves are responsible for the precipitation of $E > 30$ keV electrons in both regions.

Citation: Meredith, N. P., R. B. Horne, M. M. Lam, M. H. Denton, J. E. Borovsky, and J. C. Green (2011), Energetic electron precipitation during high-speed solar wind stream driven storms, *J. Geophys. Res.*, *116*, A05223, doi:10.1029/2010JA016293.

1. Introduction

[2] Precipitating energetic electrons produce odd nitrogen (NO_x) in the Earth's mesosphere and thermosphere. NO_x is rapidly destroyed by sunlight, but, during polar winters, when there is little or no sunlight around, the precipitation can lead to the build up of substantial amounts of NO_x at these altitudes. When combined with a strong polar vortex, which isolates the polar air from mid latitudes, downward vertical transport can lead to the appearance of significant amounts of NO_x in the upper stratosphere [*Callis et al.*, 1996; *Siskind et al.*, 2000; *Randall et al.*, 2005, 2006; *Clilverd et al.*, 2006, 2007]. Here it can have a significant effect on the ozone content, since NO_x destroys odd oxygen through catalytic reactions [*Lary*, 1997; *Grenfell et al.*, 2006]. Indeed, a recent chemistry-climate model suggests that energetic particle precipitation can lead to annual ozone decreases of up to 30% in the polar stratosphere [*Rozanov et al.*, 2005], leading to a cooling of up to 2 K in the polar middle stratosphere, together with detectable changes in temperature at the surface of the Earth. *Seppälä et al.* [2009] recently discovered a link between geomagnetic activity and polar surface air temperatures, with differences of the order of ±4.5 K between magnetically quiet and active years depending on location. These results are consistent with the model results of *Rozanov et al.* [2005], suggesting that energetic particle precipitation from the inner magnetosphere may affect surface level climate.

[3] Which range of electron energies is most important for atmospheric chemistry remains a question of debate. Higher-energy electrons penetrate down to lower altitudes but there are fewer of them. Highly relativistic electrons with energies greater than ~3 MeV typically penetrate down to the upper stratosphere [e.g., *Turunen et al.*, 2009] where they may produce NO_x in situ. Lower-energy electrons cannot reach the upper stratosphere directly and so any NO_x they produce needs downward transport to reach the upper stratosphere. Auroral electrons with energies in the range 100 eV < E < 30 keV only penetrate as far as the lower

[1]British Antarctic Survey, Natural Environment Research Council, Cambridge, UK.
[2]Department of Physics and Astronomy, University of Leicester, Leicester, UK.
[3]Department of Physics, Lancaster University, Lancaster, UK.
[4]Space Science and Applications, Los Alamos National Laboratory, Los Alamos, New Mexico, USA.
[5]Space Weather Prediction Center, National Oceanic and Atmospheric Administration, Boulder, Colorado, USA.

0148-0227/11/2010JA016293

Table 1. NOAA POES Satellites Used in This Study

Satellite	Altitude (km)	Inclination (deg)	Period (min)	LTAN	Data Window
NOAA-15	807	98.5	101.1	16:50	01/07/98–31/12/07
NOAA-16	849	99.0	102.1	17:31	10/01/01–31/12/07
NOAA-17	810	98.7	101.2	21:34	12/07/02–31/12/07
NOAA-18	854	98.7	102.1	13:41	07/06/05–31/12/07

thermosphere and require significant downward transport. Higher-energy electrons, $E > 30$ keV, associated with substorm injections and the Van Allen radiation belts, deposit most of their energy in the mesosphere and, subsequently, require less downward transport. Recent ground-based observations of NO_x show that direct production by 300 keV electrons occurs during storms (D. A. Newnham et al., Direct observations of nitric oxide produced by ~300 keV energetic electron precipitation in the Antarctic middle atmosphere, submitted to *Geophysical Research Letters*, 2010) but, in general, observations suggest that both auroral and high-energy sources may be important, depending on geomagnetic conditions [*Clilverd et al.*, 2007, 2009].

[4] Particle precipitation increases during enhanced geomagnetic activity driven by the Sun. There are two principle solar drivers: coronal mass ejections (CMEs), which lead to episodic storms that peak during solar maximum [*St. Cyr et al.*, 2000], and coronal holes which produce recurrent high-speed solar wind streams (HSSs) that peak during the declining phase of the solar cycle [*Burlaga and Lepping*, 1977; *Gonzalez et al.*, 1999]. The largest geomagnetic storms, as monitored by the *Dst* index, are driven by interplanetary coronal mass ejections. Such storms typically have a minimum *Dst* of less than −100 nT and are associated with recovery phases of the order of a couple of days. HSS-driven storms evoke a much smaller response in *Dst*, with an average minimum *Dst* of −40 nT [*Richardson et al.*, 2006]. However, they have much more extensive recovery phases, typically lasting from 5–10 days, and, as a result, may deposit more energy in the magnetosphere than larger CME-driven storms [*Kozyra et al.*, 2006; *Turner et al.*, 2006].

[5] *Horne et al.* [2009] recently conducted a survey of precipitating energetic electrons during the different phases of moderate and stronger geomagnetic storms, which are largely driven by interplanetary coronal mass ejections, using more than 9 years of low-altitude satellite data. On average, the flux of precipitating relativistic ($E > 1$ MeV) electrons was found to be roughly the same during the prestorm and main phase and subsequently increased during the recovery phase. This suggests that, during CME-driven storms, the observed main phase reduction in the trapped flux of relativistic electrons, commonly referred to as the "drop out", is not due to precipitation to the atmosphere. Instead, the flux of precipitating relativistic electrons peaks during the recovery phase, at the same time as the trapped flux is also generally increasing. In this study we examine storms that have their origin in coronal holes, the other major solar driver, to see whether relativistic electron flux dropouts associated with HSS-driven storms [*Borovsky and Denton*, 2009a; *Morley et al.*, 2010a] could be caused by precipitation to the atmosphere.

[6] Rapid Alfvénic magnetic field fluctuations occur within high-speed streams [*Tsurutani et al.*, 1995] leading to intermittent intervals of enhanced magnetospheric convection and repetitive substorm activity [*Lyons et al.*, 2009]. Enhanced levels of convection and substorm activity inject subrelativistic particles into the Earth's inner magnetosphere leading to the generation of a rich variety of plasma waves, including electron cyclotron harmonic (ECH) waves [*Scarf et al.*, 1973; *Meredith et al.*, 2009], whistler mode chorus [*Tsurutani and Smith*, 1974, 1977; *Lauben et al.*, 1998; *Meredith et al.*, 2001, 2009; *Li et al.*, 2009], plasmaspheric hiss [*Smith et al.*, 1974; *Thorne et al.*, 1974, 1977; *Meredith et al.*, 2004; *Bortnik et al.*, 2008, 2009], magnetosonic waves [*Meredith et al.*, 2008], and electromagnetic ion cyclotron waves [*Fraser et al.*, 2010]. These waves can violate the first and second adiabatic invariants leading to energy diffusion and pitch angle scattering [*Horne and Thorne*, 1998; *Shprits*, 2009]. For example, whistler mode chorus is largely responsible for the pitch angle scattering and loss of low-energy plasma sheet electrons and as such is responsible for the production of both the diffuse aurora [*Thorne et al.*, 2010] and the pulsating aurora [*Nishimura et al.*, 2010]. At higher energies, whistler mode chorus, plasmaspheric hiss and electromagnetic ion cyclotron (EMIC) waves all contribute to pitch angle scattering and the subsequent loss of relativistic electrons [*Millan and Thorne*, 2007]. Whistler mode chorus and magnetosonic waves may also lead to significant energy diffusion which can give rise to local electron acceleration [*Horne et al.*, 2005a, 2005b, 2007].

[7] In view of the importance of energetic particle precipitation to atmospheric chemistry, here we conduct a superposed epoch analysis of 42 HSS-driven storms using electron data from four National Oceanic and Atmospheric Administration (NOAA) Polar Orbiting Environmental Satellites (POES) (section 2). We first examine the temporal evolution of the precipitation through the different phases of the storm to see when the precipitation is likely to be strongest and, in particular, whether relativistic electron precipitation is enhanced during the flux drop out (section 3). We then study the geographic extent of the precipitation to see where the precipitation occurs in relation to the polar vortex (section 4). We also map the precipitating particles to the magnetic equatorial plane, where the pitch angle scattering occurs, to comment on the likely causes of the precipitation (section 5). The results of our study are discussed in section 6 and the conclusions presented in section 7.

2. Instrumentation

[8] The particle data used in this study were collected by the Medium Energy Proton and Electron Detector (MEPED) on board the NOAA POES. These satellites orbit the Earth approximately 14 times each day in Sun-synchronous, low-altitude, polar orbits. Here we use data from NOAA-15, NOAA-16, NOAA-17, and NOAA-18 (Table 1).

[9] The MEPED instrument includes two electron solid-state detector telescopes that measure the flux of electrons in three energy bands in the range 30–2500 keV and two proton solid-state detector telescopes that measure the flux of protons in the energy range 30–6900 keV [*Evans and Greer*, 2004]. For each detector telescope pair, one, called the "0°" telescope, T0, is aligned such that the center of its field of view is rotated 9° from the direction outward along the local zenith. The other, called the "90°" telescope, T90,

is mounted perpendicular to T0 such that the center axis of its field of view is rotated 9° from the direction antiparallel to the direction of the spacecraft velocity. Since the field of view of each telescope is 30°, the T0 telescope measures precipitating flux inside the bounce loss cone for $L > 1.4$ [*Rodger et al.*, 2010a]. At 55°–68° invariant latitude, on field lines that map to the outer radiation belt, the T90 detector measures a mix of particles which may be in the bounce or drift loss cone or stably trapped [*Rodger et al.*, 2010b]. For a given L shell in this region, when averaged over all geographic longitudes, the stably trapped particle fluxes will tend to dominate the average fluxes, and we henceforth refer to these average fluxes as the trapped fluxes. We use data from the $30 < E < 2500$ keV, the $100 < E < 2500$ keV, and the $300 < E < 2500$ keV electron channels, which we henceforth refer to as the $E > 30$ keV, $E > 100$ keV and $E > 300$ keV channels, respectively. We also use data from the $E > 6900$ keV proton channel which responds to relativistic electrons with energies $E > 1$ MeV [e.g., *Sandanger et al.*, 2009]. Data from each detector are accumulated for 1 s and, since the electronics are shared between the two detectors, data from each detector are collected at a 2 s time resolution.

3. Superposed Epoch Analysis

[10] To assess the general behavior of the trapped and precipitating energetic electrons during HSS-driven storms, we conducted a superposed epoch analysis of 42 HSS storms that occurred between 2003 and 2005. The storms were selected by examining the solar wind velocities and seeking intervals of east-west flow deflection followed by sustained elevated solar wind speed, and correspond to the subset of the 124 HSS storms used successfully in the studies of the magnetospheric response to HSSs [*Borovsky and Denton*, 2008, 2009a, 2009b; *Denton and Borovsky*, 2008, 2009; *Denton et al.*, 2009, 2010] which occurred after the launch of NOAA-15 in 1998. The zero epoch for each storm was taken to be the time of storm convection onset. This "onset" time was initially detected by a strong increase in the *Kp* index [cf. *Elphic et al.*, 1999; *Thomsen*, 2004], and subsequently refined to a 30 minute resolution using changes in the Midnight Boundary Index [*Madden and Gussenhoven*, 1990].

[11] The flux measurements from the electron detector telescopes were initially corrected for proton contamination by excluding solar proton events and correcting for ring current protons as described by *Lam et al.* [2010]. Since the electron flux falls rapidly with increasing energy we ensured that the $E > 30$ keV flux was greater than the $E > 100$ keV flux which was in turn greater than the $E > 300$ keV flux to exclude bit errors. The sensor response of the $E > 6900$ keV proton channel used to monitor relativistic electrons with energies $E > 1$ MeV is not well characterized, and, consequently, the data from this channel were left in counts per second. Solar proton events were again excluded and we confirmed that the $E > 6900$ keV channel was responding to relativistic electrons by ensuring that the counts in the $E > 6900$ keV proton channel were greater than those in the $2500 < E < 6900$ keV proton channel. The POES electron data were then binned as a function of UT time and McIlwain L shell at a resolution of 1 h in time and 0.1 L by combining data from all available satellites. The McIlwain L value at the satellite location was calculated using the International Geomagnetic Reference Field model of the magnetic field for the midpoint of the appropriate year and the National Space Science Data Center INVAR program. The solar wind parameters and the geomagnetic indices were stored at the same temporal resolution. The binned data were subsequently analyzed to produce average fluxes or count rates depending on energy channel, and averaged geophysical parameters as a function of epoch time. Figure 1 shows the results of the superposed epoch analysis. Figures 1a–1k show the T90 and T0 measurements for electrons with energies $E > 1$ MeV, $E > 300$ keV, $E > 100$ keV, and $E > 30$ keV, the solar wind speed and the interplanetary magnetic field (IMF) north-south component (*Bz*) in GSM coordinates, the *Dst* index (color-coded), and the *Kp* index (color-coded) together with a trace of the *AE* index, respectively. Line plots of the T0 and T90 measurements for each of the four energy channels are plotted in a similar format in Figure 2. Here line plots of the measurements at $L = 4$, $L = 5$, and $L = 6$, coded green, black, and red, respectively, are shown for each of the detectors and each of the energy ranges. The solar wind parameters and geophysical indices are plotted for reference in Figures 2i–2k in the same format as for Figure 1.

[12] The 5 days before storm onset are characterized by low solar wind speeds (red trace, Figure 1i). The speed decreases from 510 km s^{-1} 5 days before storm onset to 370 km s^{-1} at an epoch time, t_e, of −0.8 days. The solar wind speed then starts to increase, reaching 450 km s^{-1} at storm onset. The IMF *Bz* (black trace, Figure 1i) fluctuates about zero from $t_e = -5$ to −2 days but then becomes predominantly northward, before swinging abruptly southward at storm onset. The high-speed stream itself typically lasts for 5 days, with velocities exceeding 500 km s^{-1} from $t_e = +0.5$ to $t_e = +5$ days. The IMF is predominantly weakly southward for the entire 5 day interval of the high-speed stream. The geomagnetic activity indices (Figures 1j and 1k) all record decreasing activity from $t_e = -5$ to $t_e = -0.25$ days. From $t_e = -0.25$ days to storm onset the *Dst* index becomes weakly positive and the *AE* and *Kp* activity start increasing. Peak *AE* and *Kp* activity occurs close to storm onset whereas the *Dst* index becomes most disturbed at around $t_e = +0.5$ days. Following peak activity the activity indices subsequently gradually decline with time, returning to prestorm levels about 5 days after storm onset.

[13] The fluxes of trapped electrons with energies $E > 30$ keV, $E > 100$ keV, and $E > 300$ keV, shown in Figures 1g, 1e, and 1c, respectively, generally decrease with time in the 5 days prior to storm onset. In contrast, the trapped relativistic electron count rate (Figure 1a) remains roughly constant during this interval. In the first few hours following storm onset, the flux of trapped $E > 30$ keV electrons increases dramatically, with the effect first being seen at larger L (Figure 2g). The fluxes of these electrons subsequently remain enhanced, albeit with some variability, during the high-speed solar wind stream. The flux of trapped $E > 100$ keV electrons also begins to rise in the first few hours following storm onset, but the rise is much more gradual, peaking roughly 2 days later and then gradually falling off with time (Figure 2e). At higher energies there is a reduction in the flux of trapped $E > 300$ keV electrons, which is most prominent at high L (Figure 2c). The minimum

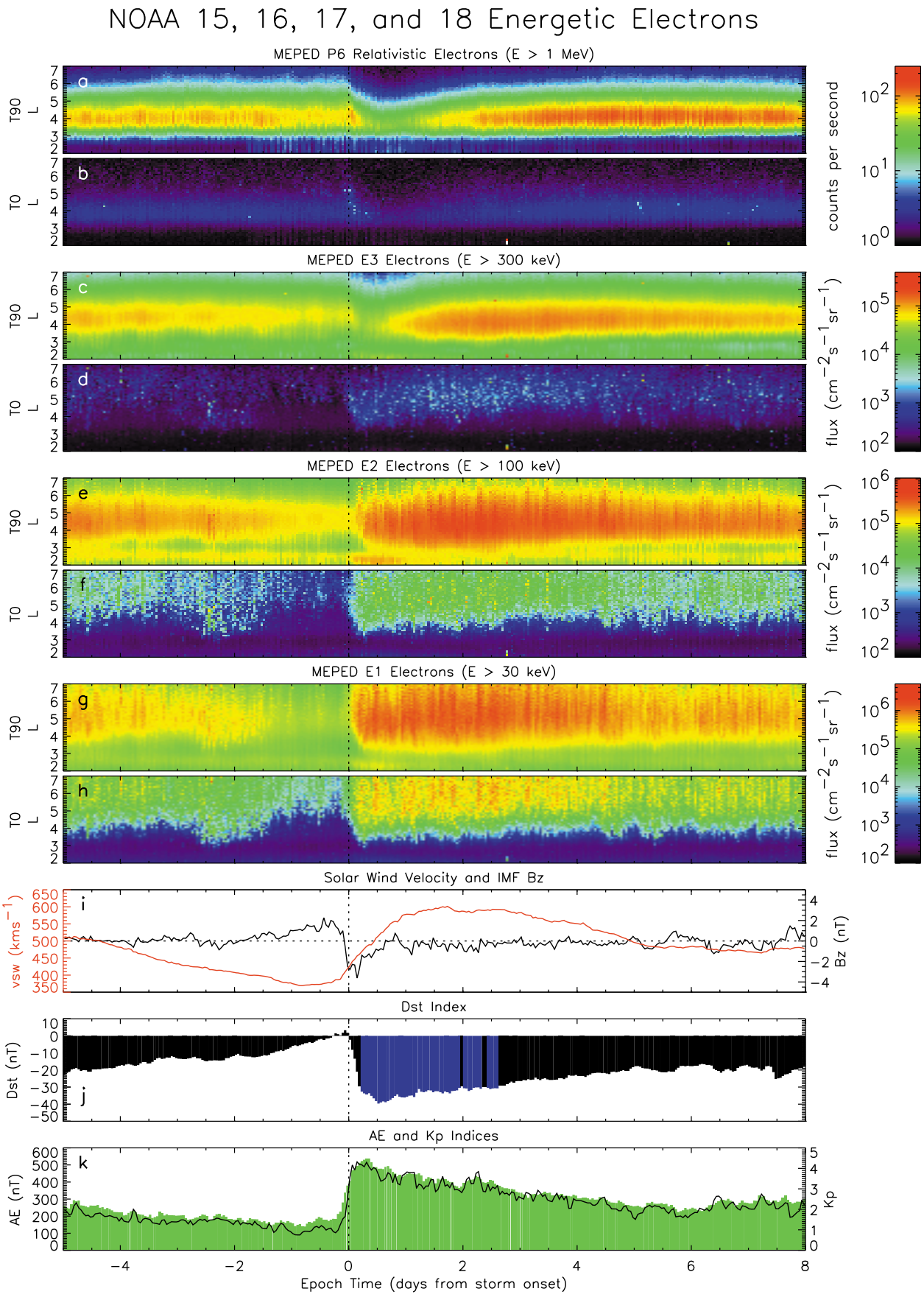
NOAA 15, 16, 17, and 18 Energetic Electrons
MEPED P6 Relativistic Electrons (E > 1 MeV)
MEPED E3 Electrons (E > 300 keV)
MEPED E2 Electrons (E > 100 keV)
MEPED E1 Electrons (E > 30 keV)
T90
T0
L
counts per second
flux (cm^{-2}s^{-1}sr^{-1})
Solar Wind Velocity and IMF Bz
vsw (kms^{-1})
Bz (nT)
Dst Index
Dst (nT)
AE and Kp Indices
AE (nT)
Kp
Epoch Time (days from storm onset)

Figure 1

in the flux is seen approximately 0.5 days following storm onset and is coincident with the minimum in the *Dst* index. The flux of trapped $E > 300$ keV electrons subsequently increases, peaking 2–4 days later, depending on L, and then gradually falling off with time. The trapped relativistic electron count rate falls by a factor of ~3 following storm onset (Figure 2a). This reduction in count rate, referred to as the flux drop out, occurs across the entire outer radiation belt with the minimum count rate being seen roughly 0.5 days following storm onset. The trapped relativistic electron count rate subsequently begins to increase, peaking roughly 5 days following storm onset. The largest increases are observed in the heart of the outer radiation belt ($4 < L < 5$) where the pre/post storm ratio of trapped relativistic electrons is ~1.5. However, further out, at $L = 6.0$, the pre and post storm levels are roughly similar.

[14] The fluxes of precipitating electrons with energies $E > 30$ keV, $E > 100$ keV, and $E > 300$ keV, shown in Figures 1h, 1f, and 1d, respectively, generally decrease with time in the 5 days prior to storm onset, and, in particular, reach very low levels inside $L = 5.0$ in the 1.5 day interval before storm onset. This 1.5 day period before the onset of the HSS has been identified as the "calm before the storm" [*Borovsky and Steinberg*, 2006]. The fluxes of precipitating energetic electrons with energies $E > 30$ keV, $E > 100$ keV, and $E > 300$ keV increase dramatically at storm onset. The increase in the precipitating flux is roughly 3, 2, and 1 order of magnitude at $E > 30$ keV (Figure 2h), $E > 100$ keV (Figure 2f), and $E > 300$ keV (Figure 2d), respectively. The sensitivity to precipitating relativistic electrons is low and their count rate typically only rises above the noise level in the region $3 < L < 5$ (Figure 1b). Here the precipitating relativistic electron count rate stays roughly constant in the 5 days prior to storm onset (Figure 1b). The precipitating relativistic electron count rate subsequently decreases and reaches a minimum about 0.5 days after storm onset. Crucially, there is no evidence for enhanced precipitation during the interval when the trapped count rate falls most rapidly, suggesting that the "drop out" in the count rate of the trapped particles is not due to losses to the atmosphere. The precipitating count rate subsequently begins to increase, peaking roughly 5 days following storm onset at levels slightly higher than the prestorm level (Figure 2b).

[15] At $L = 4$ the superposed data stay above the noise level for the entire period enabling us to calculate the ratio of the precipitating to trapped count rate in the heart of the outer radiation belt. However, it is important to subtract the background noise before calculating this ratio since the T0 count rates are only just slightly above the noise level during the storm main phase. From the superposed epoch data at $L = 8.5$, where the relativistic electrons are below the level of detectability for both the T0 and T90 detector telescopes, the noise level for both detector telescopes is determined to be 1.2 counts per second. The ratio $T0_b/T90_b$, where the subscript b denotes that the background noise has been subtracted, at $L = 4$ is shown in blue in Figure 2b and stays roughly constant during the entire period.

[16] The statistical properties of a representative selection of the parameters used in the superposed epoch analysis are shown in Figure 3. Figures 3a–3k show the T90 and T0 $E > 1$ MeV count rates at $L = 4$, the T90 and T0 $E > 300$ keV, $E > 100$ keV, and $E > 30$ keV electron fluxes at $L = 5$, the solar wind speed, the *Dst* index and the *Kp* index, respectively. The drop out in the count rate of the trapped relativistic electrons following storm onset (Figure 3a) and the concomitant decrease in the count rate of the precipitating relativistic electrons (Figure 3b) is seen in the traces of the mean, the upper and lower quartiles and in the envelope showing the range between the 10th to the 90th percentile, indicating that this is a robust result. During the passage of the high-speed stream, the mean and the upper quartile of the electron measurements show a broadly similar response, with the mean of the T0 and T90 measurements lying slightly above and slightly below the upper quartile, respectively.

4. Geographic Distribution of Electron Precipitation

[17] To determine the geographic distribution of the precipitation during and preceding HSS-driven storms we divided the storms into three intervals which we define as: the calm before the storm ($-2 < t_e < 0$ days), the main phase/early recovery phase ($0 < t_e < 2$ days), and the extended recovery phase ($2 < t_e < 5$ days). We subsequently binned the data as a function of geographic latitude and geographic longitude for these three time intervals in steps of 1° in latitude and 5° in longitude. It should be noted that these geographic maps show where the precipitation falls on average throughout the selected time intervals for each of the 42 HSS-driven storms and thus do not represent an instantaneous "snap shot" of auroral precipitation. The actual geographic extent of the precipitation at any given instant in time typically varies with local time and this is averaged out in the analysis.

[18] Figure 4 (top) shows the distribution of precipitating energetic E > 30 keV electrons in the northern hemisphere. From left to right the results are shown for the calm before the storm, the main phase/early recovery phase, and the extended recovery phase. The solid white line in each panel represents the typical latitude of the maximum zonal wind of the wintertime stratospheric polar vortex [*Randel et al.*, 2004]. The E > 30 keV electron precipitation is confined to an oval, which ranges in latitudinal extent from 65°N to 80°N at a longitude of 90°E to 50°N–65°N at a longitude of 270°E. The corresponding results for the southern hemisphere are shown in Figure 4 (bottom) in the same format. Here, the precipitation is again confined to an oval which ranges in latitudinal extent from 70°S to 85°S at a longitude of 315°E to 45°S–60°S at a longitude of 135°E. During the calm before the storm low-precipitating fluxes, of the order 2×10^4 cm^{-2} s^{-1} sr^{-1}, are seen in the oval at all geographic longitudes, in both hemispheres. The precipitating fluxes dramatically increase following storm onset and are typi-

Figure 1. Superposed geomagnetic indices, solar wind parameters, and POES energetic electrons during the 42 HSS-driven storms. (a–k) The T90 and T0 measurements for the $E > 1$ MeV, $E > 300$ keV, $E > 100$ keV, and $E > 30$ keV electrons, the solar wind speed and IMF *Bz* (GSM), the *Dst* index (color-coded), and the *Kp* index (color-coded) together with a trace of the *AE* index, respectively.

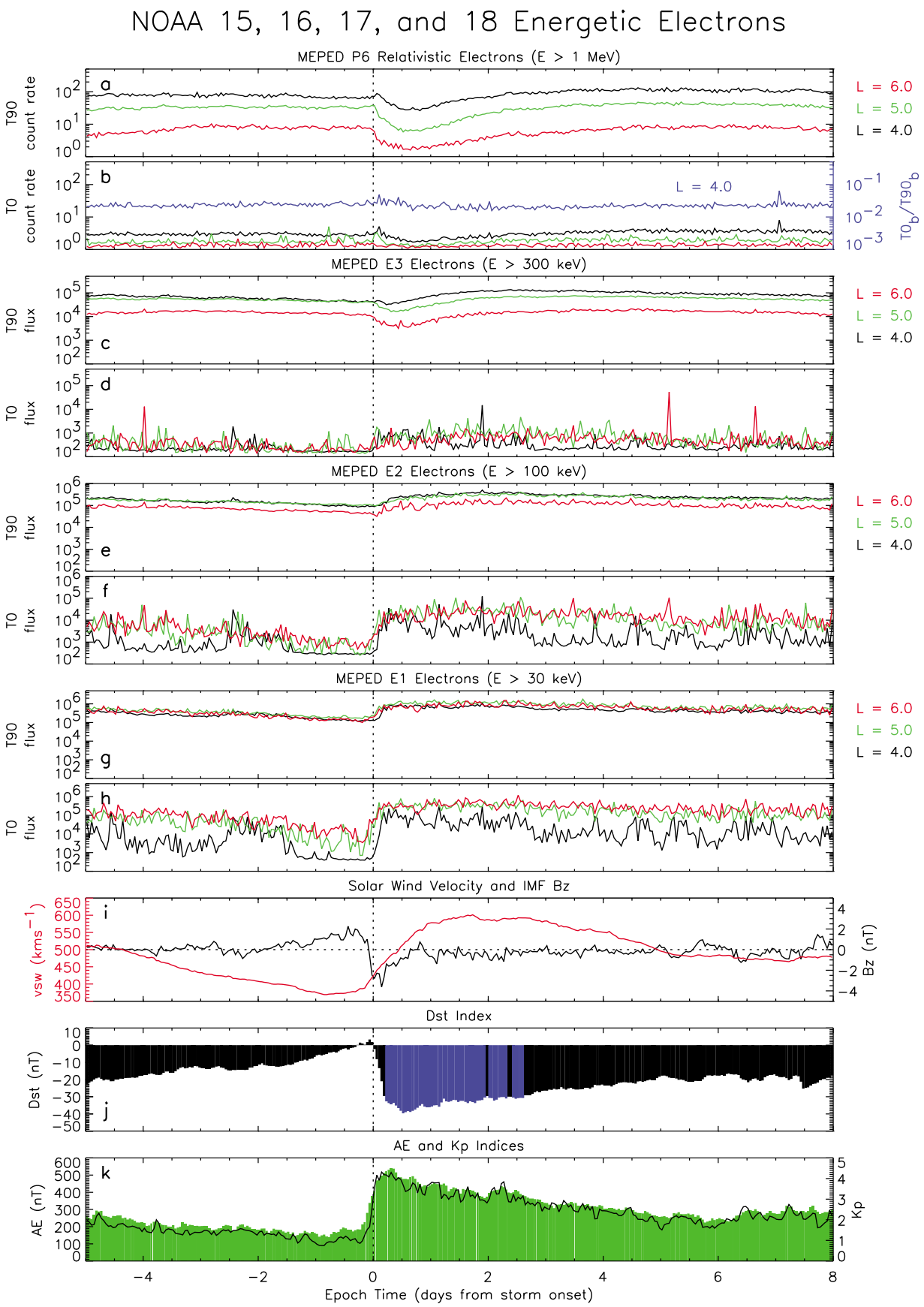
NOAA 15, 16, 17, and 18 Energetic Electrons
MEPED P6 Relativistic Electrons (E > 1 MeV)
T90 count rate
T0 count rate
L = 4.0
$T0_b/T90_b$
MEPED E3 Electrons (E > 300 keV)
T90 flux
T0 flux
MEPED E2 Electrons (E > 100 keV)
MEPED E1 Electrons (E > 30 keV)
L = 6.0
L = 5.0
L = 4.0
Solar Wind Velocity and IMF Bz
vsw (kms^{-1})
Bz (nT)
Dst Index
Dst (nT)
AE and Kp Indices
AE (nT)
Kp
Epoch Time (days from storm onset)

Figure 2

cally an order of magnitude higher at all geographic longitudes in the oval, in both hemispheres, during both the main phase/early recovery phase and the extended recovery phases. In the northern (southern) hemisphere roughly 80% (75%) of the total hemispheric precipitation falls within the wintertime stratospheric polar vortex.

[19] Figure 5 (top) shows the distribution of precipitating relativistic electrons in the northern hemisphere in the same format as Figure 4. Weak precipitation, of the order 1 count per second, occurs in a narrow latitudinal band, 5°–10° wide, which extends, continuously, in longitude from 135°E, where the band extends from 65°N–70°N to 285°E, where the band extends from 55° to 65°. The corresponding results for the southern hemisphere are shown in Figure 5 (bottom). The strongest precipitating relativistic electron count rate is seen in a broad latitude band, roughly 10° wide, which extends, continuously, in longitude from 315°E to 30°E. Here the count rate typically exceed 5 counts per second, approximately 5 times larger than the largest precipitation in the northern hemisphere. Weaker precipitation, of the order of a few counts per second, are seen at longitudes extending to 180°E and 90°E, respectively. There is very little relativistic electron precipitation at longitudes between 90°E and 180°E. In contrast to the $E > 30$ keV precipitation, the smallest count rate is seen during the main/early recovery phase. The intensity and geographic distribution of the precipitating relativistic electrons in the southern hemisphere are fairly similar in the calm before the storm and during the extended recovery phase.

5. Distribution of Electron Precipitation as a Function of *L* and *MLT*

[20] Wave-particle interactions leading to the pitch angle scattering and subsequent loss to the atmosphere of energetic electrons typically take place in the geomagnetic equatorial plane. In order to determine the location of these interactions during and preceding high-speed solar wind streams we divided the storm into the three intervals as defined above, and subsequently rebinned the data as a function of L shell and magnetic local time (MLT) in steps of 0.1 L and 1 h in local time.

[21] Figure 6 (top) shows the precipitating E > 30 keV electrons as a function of L and MLT. This map was constructed using all the relevant data from both hemispheres since enhanced fluxes of precipitating $E > 30$ keV particles are seen in both hemispheres and at all geographic longitudes. From left to right the results are shown for the calm before the storm, the main phase/early recovery phase, and the extended recovery phase. Low fluxes of precipitating $E > 30$ keV elecrons are seen in the calm before the storm with the bulk of the albeit weak precipitation occurring in the prenoon sector over a range of L shells L > 5. The most intense precipitation is seen following storm onset with fluxes exceeding 3×10^5 cm^{-2} s^{-1} sr^{-1} from 21:00 MLT through dawn to 13:00 MLT. Near midnight the peak of the precipitation occurs in the range $4.5 < L < 7$. The outermost extent of the precipitation increases with increasing MLT and typically extends out to $L = 9$ in the prenoon sector. There is very little precipitation near dusk at any L.

[22] At higher energies, it is not possible to extract the variation with L and MLT of the precipitating relativistic electron count rate because the count rates are too low and the statistics too poor to bring out any consistent variation with L and MLT. However, we can obtain information on the location of the strongest wave-particle interactions causing the precipitation by looking at the L, MLT distribution of the $E > 1$ MeV electrons freshly deposited into the drift loss cone. For field lines that map to the heart of the outer radiation belt, electrons freshly deposited into the drift loss cone are observed by the T90 detector at magnetic longitudes in the range 160–190°E. Figure 6 (bottom) shows the T90 E > 1 MeV electron count rates observed at these magnetic longitudes as a function of L and MLT in the same format as the top images. During the calm before the storm and the main/early recovery phase the strongest count rates are seen in the region $3.5 < L < 5$ from 1000 to 1900 MLT. The largest count rates are seen during the extended recovery phase in the region $3.5 < L < 5$ and cover a larger region of geospace from roughly 0500 MLT to 2100 MLT.

6. Discussion

[23] The main phase of HSS-driven storms is associated with a drop out in the flux of trapped relativistic electrons [*Borovsky and Denton*, 2009a; *Morley et al.*, 2010a], as evidenced in our study by the reduction in the trapped relativistic electron count rate across a wide range of L following storm onset (Figure 2a). Determining the cause of this drop out is a major, outstanding question in radiation belt physics [e.g., *Denton et al.*, 2008]. The drop out has traditionally been thought to be caused by a combination of adiabatic change associated with the decrease in *Dst* [*Kim and Chan*, 1997], together with pitch angle scattering and subsequent loss to the atmosphere [*Millan and Thorne*, 2007], outward drift and loss to the magnetopause [*Li et al.*, 1997; *Shprits et al.*, 2006], and, more recently, nonlinear decreases in energy, referred to as advection (J. Albert, personal communication, 2010). Our results show that the dropout of the trapped relativistic electrons during HSS-driven storms is not caused by pitch angle scattering and subsequent loss to the atmosphere since the precipitating relativistic electrons also drop out and, during the drop out, the ratio $T0_b/T90_b$ in the heart of the outer radiation belt at $L = 4$ stays roughly constant.

[24] Increases in the flux of relativistic electrons in the Earth's outer radiation belt have long been known to be well correlated with high-speed solar wind streams [*Paulikas and Blake*, 1979; *Baker et al.*, 1997; *Blake et al.*, 1997; *Li et al.*, 1997; *O'Brien et al.*, 2001; *Iles et al.*, 2002], and, indeed,

Figure 2. Superposed geomagnetic indices, solar wind parameters, and POES energetic electrons during the 42 HSS-driven storms. (a–k) Line plots of the T90 and T0 measurements for $E > 1$ MeV, $E > 300$ keV, $E > 100$ keV, and $E > 30$ keV electrons, the solar wind speed and IMF *Bz* (GSM), the *Dst* index (color-coded), and the *Kp* index (color-coded) together with a trace of the *AE* index, respectively. The traces in the line plots show the associated measurements at $L = 4$, $L = 5$, and $L = 6$ and are colored black, green, and red, respectively. The blue trace in Figure 2b shows the ratio $T0_b/T90_b$, where the subscript b denotes that the background noise has been subtracted for each detector telescope, at $L = 4$ for $E > 1$ MeV electrons.

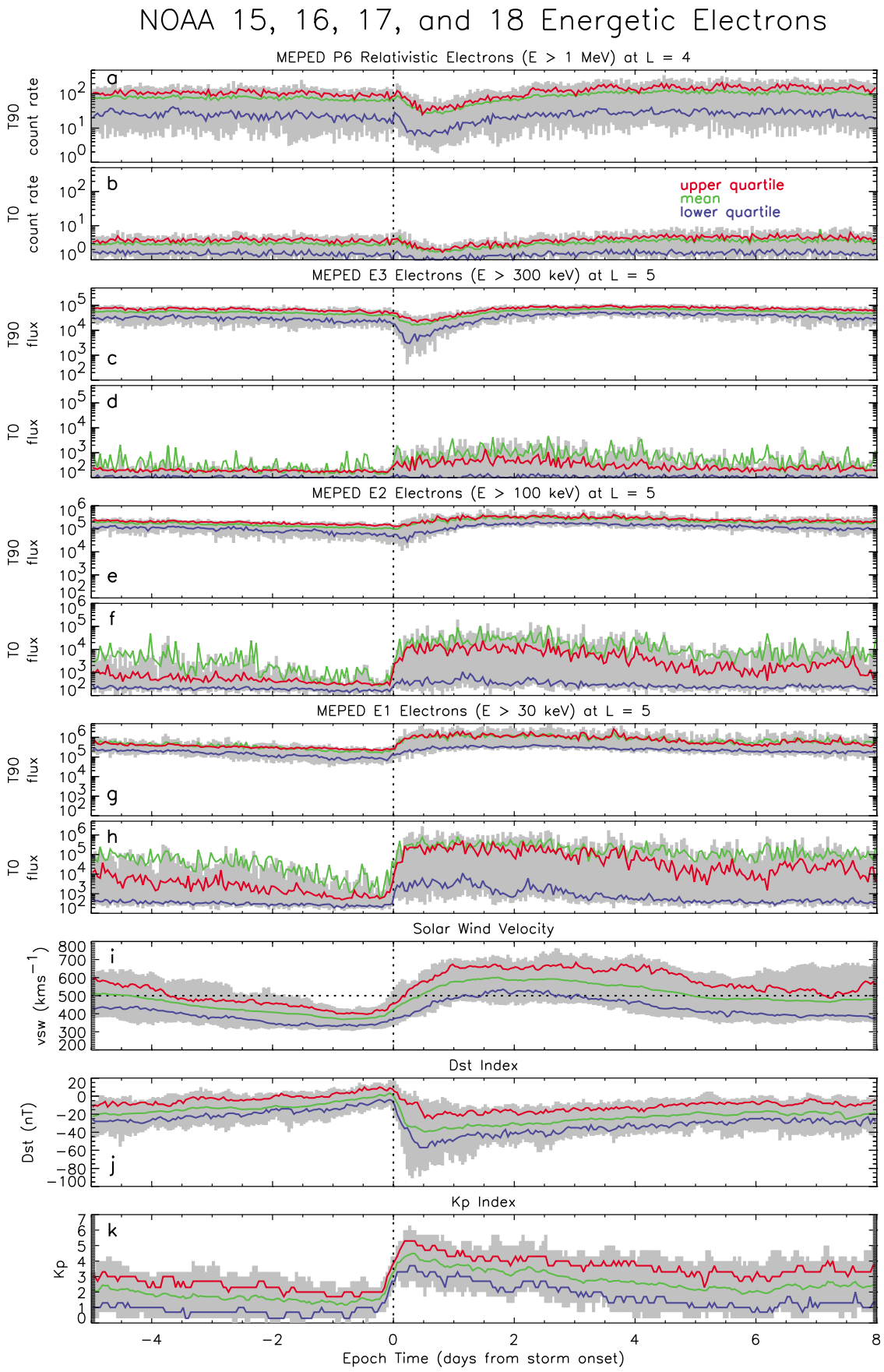
NOAA 15, 16, 17, and 18 Energetic Electrons
MEPED P6 Relativistic Electrons (E > 1 MeV) at L = 4
T90 count rate
T0 count rate
upper quartile
mean
lower quartile
MEPED E3 Electrons (E > 300 keV) at L = 5
T90 flux
T0 flux
MEPED E2 Electrons (E > 100 keV) at L = 5
MEPED E1 Electrons (E > 30 keV) at L = 5
Solar Wind Velocity
vsw (kms^{-1})
Dst Index
Dst (nT)
Kp Index
Kp
Epoch Time (days from storm onset)

Figure 3

the flux of relativistic electrons in the outer radiation belts peak during the declining phase of the solar cycle when HSS-driven storms are most prevalent [*Li et al.*, 2001; *Miyoshi et al.*, 2004]. While individual HSS-driven storms may result in increases in the flux of relativistic electrons by an order of magnitude or more [e.g., *Baker et al.*, 1994, 1997; *Lam et al.*, 2009], superposed epoch analyses tend to show that, on average, the flux of relativistic electrons at geosynchronous orbit is generally a factor of 2–3 times larger following the passage of a geoeffective high-speed solar wind stream [*Borovsky and Denton*, 2009a; *Miyoshi and Kataoka*, 2008]. Our study shows that, on average, the poststorm flux of trapped relativistic electrons at low altitudes on field lines that map to the heart of the outer radiation belt ($4 < L < 5$) is roughly 1.5 times the prestorm flux. Further out, at $L = 6$, we find little difference between the pre and post storm flux levels. Our results are broadly consistent with those of *Morley et al.* [2010a] who, from a superposed epoch analysis of 67 solar wind stream interfaces using global positioning system observations, found only a small net increase in the counts of 0.77–1.25 MeV electrons in the heart of the outer radiation belt and no increase at $L^* = 6.5$. Given that individual HSS-driven storms may increase the flux of relativistic electrons by an order of magnitude or more, the question one might pose is why do superposed epoch analyses only reveal relatively small increases in the flux of trapped relativistic electrons? During periods of extreme calm, such as occurred in spring 2004 and during large parts of 2009, the trapped relativistic electron count rate measured by POES in the heart of the outer radiation belt fell to values of the order of a few counts per second. The elevated fluxes of trapped relativistic electrons typically seen following HSS-driven storms are thus roughly 2 orders of magnitude higher than the quiet time values. The reason why superposed epoch analyses of HSS-driven storms tend to report relatively small increases in the flux of trapped relativistic electrons is because, on average, the prestorm fluxes are already elevated relative to their quiet time levels. This is due to the persistence of the relativistic electron flux from previous HSS and/or CME driven storms. During the declining phase of the solar cycle, when there are often two HSS-driven storms per solar rotation [e.g., *Baker et al.*, 1997] each repeating at the 27 day synodic rotation period of the Sun, the typical interval between storms is about 14 days and the flux of relativistic electrons doesn't have enough time to relax to quiet time levels. High levels of relativistic electron fluxes can then be maintained during the declining phase of the solar cycle, even though HSS-driven storms, on average, only increase the flux by up to a factor of 2–3.

[25] The edge of the winter stratospheric polar vortex, which is typically near 60°N(S) [*Randel et al.*, 2004], is denoted by the solid white line in Figures 4 and 5. A significant fraction of the precipitation occurs inside the vortex. High-speed solar wind streams thus provide an almost continual source of energetic particle precipitation and associated NO_x inside the vortex in the mesosphere. This NO_x can be transported into the polar stratosphere in the winter polar region where NO_x has a long lifetime against photodissociation. NO_x produced in this way acts as a persistent source of NO_x for catalytic ozone destruction. Changes in ozone and the associated absorption of solar radiation in the stratosphere may result in temperature changes in the troposphere [*Rozanov et al.*, 2005; *Seppälä et al.*, 2009].

[26] The precipitating relativistic electron count rate peaks in the region poleward of the South Atlantic Anomaly (SAA). However, since the T0 detector is looking well inside the bounce loss cone at all longitudes on field lines that map to the outer radiation belt [*Rodger et al.*, 2010a], this feature is not caused by precipitation from the drift loss cone. Using a dipole field to estimate the equatorial magnetic field strength, the equatorial pitch angles measured by the T0 detector at $L = 4$ in the southern hemisphere vary from 1.5° to 3°, and are roughly 3.5° inside the bounce loss cone from 180°E, through 0°E to 90°E. If the rate of pitch angle scattering were constant with pitch angle at small pitch angles, we might expect to see similar count rates of precipitating relativistic electrons in the southern hemisphere near $L = 4$ at these longitudes. But this is not observed. Near $L = 4$ both the bounce loss cone and the equatorial pitch angle observed by the T0 detector maximize in the region poleward of the SAA. The larger precipitating relativistic electron count rate observed in this region could be due to either an increase in the rate of pitch angle diffusion with equatorial pitchangle or larger fluxes of relativistic electrons at the edge of the bounce loss cone. The latter could be caused by an anisotropic distribution function or from particles in the drift loss cone. Alternatively, it could be due to the detector looking closer to the edge of the bounce loss cone, but this would require more careful field line mapping using an accurate magnetic field model to test. The determination of the absolute level of relativistic electron precipitation to the atmosphere using POES data will require both the calculation of a realistic geometric factor for the $P > 6900$ keV channel for relativistic electrons and a very careful assessment of the pitch angle dependence inside the loss cone.

[27] There remains the possibility that the electrons could be precipitated at pitch angles greater than that measured by the T0 detector but less than the drift loss cone. However, since the flux drop out can be very rapid, of the order of a few hours or so [*Morley et al.*, 2010a], pitch angle diffusion into the loss cone may be considerably enhanced and, according to theory [*Kennel and Petschek*, 1966], precipitation should extend to smaller and smaller pitch angles. *Selesnick* [2006] and *Tu et al.* [2010] show that during the main phase of a storm the pitch angle diffusion rate is required to increase significantly to reproduce the quasi-trapped flux, i.e., the flux in the drift loss cone, which supports the

Figure 3. Statistical properties of the *Kp* and *Dst* indices, the solar wind velocity, and the POES energetic electrons used in the superposed epoch analysis. (a–k) The T90 and T0 count rates for the $E > 1$ MeV at $L = 4$, the T90 and T0 fluxes for the $E > 300$ keV, $E > 100$ keV, and $E > 30$ keV electrons at $L = 5$, the solar wind speed, the *Dst* index and the *Kp* index, respectively. In each panel the arithmetic mean and the upper and lower quartiles are coded green, red, and blue, respectively, and the range between the 10th to the 90th percentile is shaded gray.

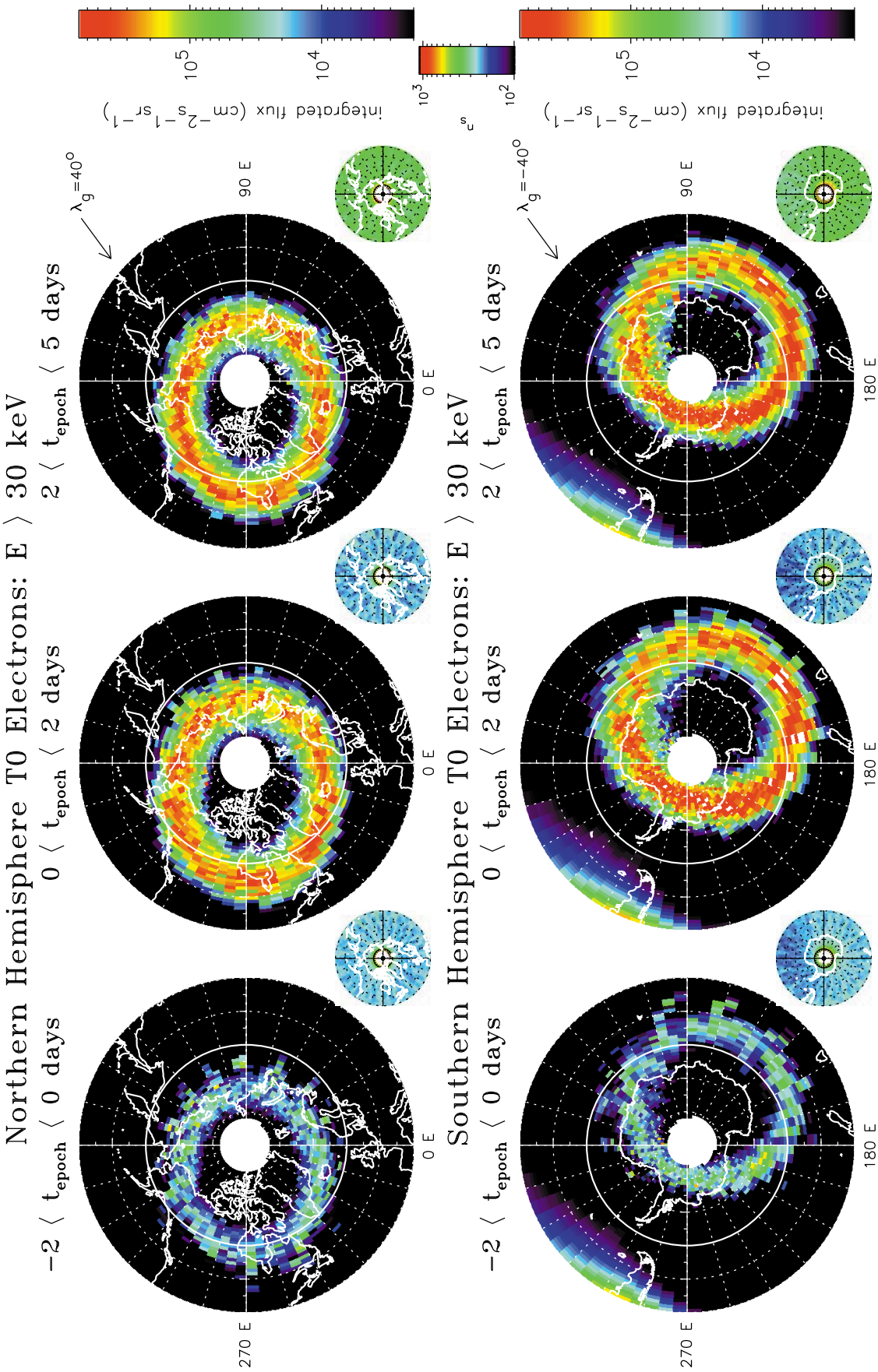

Figure 4. (top) The average integrated flux of precipitating $E > 30$ keV electrons as a function of geographic latitude and geographic longitude in the northern hemisphere for, from left to right, the calm before the storm, the main phase/early recovery phase, and the late recovery phase, respectively. (bottom) The average integrated flux of precipitating $E > 30$ keV electrons as a function of geographic latitude and geographic longitude in the southern hemisphere for the same time intervals. The solid white line on each of the plots denotes the typical equatorward extent of the polar vortex. The average integrated fluxes are shown in the large panels, and the corresponding sampling distributions are shown in the small panels.

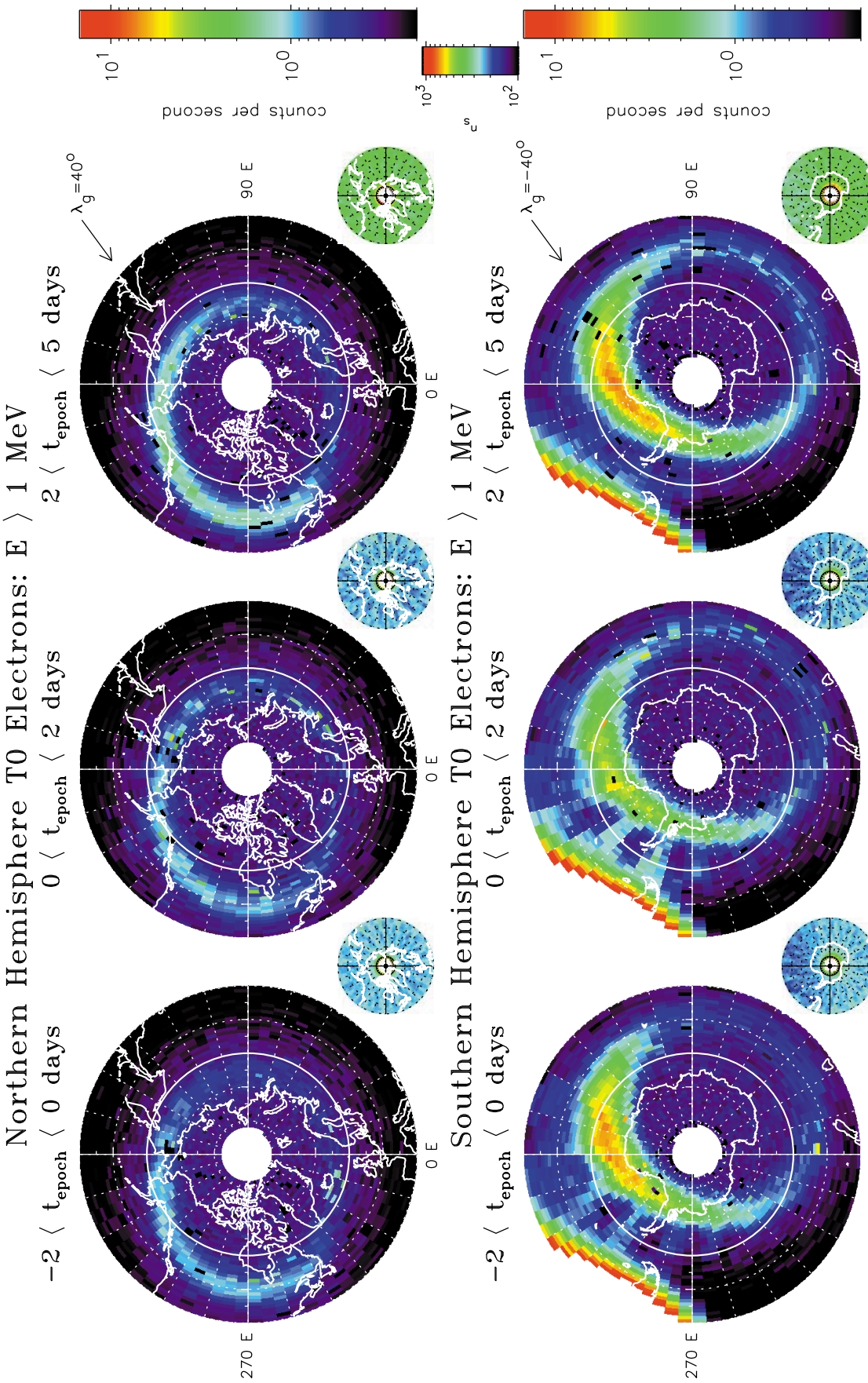

Figure 5. (top) The average count rate of precipitating $E > 1$ MeV electrons as a function of geographic latitude and geographic longitude in the northern hemisphere for, from left to right, the calm before the storm, the main phase/early recovery phase, and the late recovery phase, respectively. (bottom) The average count rate of precipitating $E > 1$ MeV electrons as a function of geographic latitude in the southern hemisphere for the same time intervals. The solid white line on each of the plots denotes the typical equatorward extent of the polar vortex. The average count rates are shown in the large panels, and the corresponding sampling distributions are shown in the small panels.

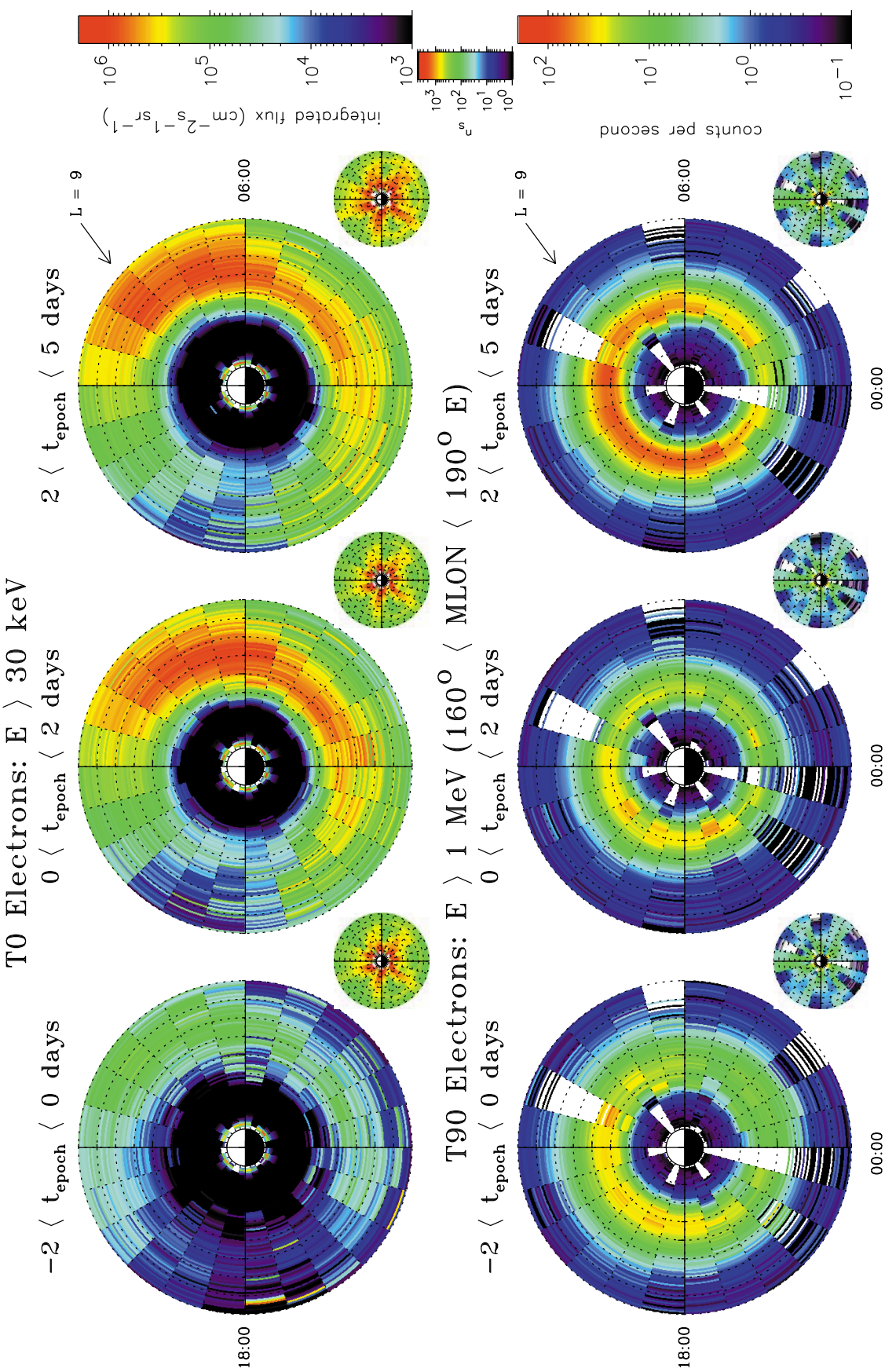

Figure 6. (top) The average integrated flux of precipitating $E > 30$ keV electrons as a function of L and MLT for, from left to right, the calm before the storm, the main phase/early recovery phase, and the late recovery phase. (bottom) The average count rate of $E > 1$ MeV electrons in the drift loss cone observed at magnetic longitudes between 160°E and 190°E as a function of L and MLT for the same time intervals. The data are shown in the large panels, and the corresponding sampling distributions are shown in the small panels.

Kennel and Petschek theory. Thus we would expect to see an increase in the T0 count rate if the flux drop outs were due to precipitation to the atmosphere, and the idea that flux drop outs would leave no signature in the T0 detector seems unlikely.

[28] The timing of the observed maximum of trapped energetic electrons associated with HSS-driven storms is energy dependent. On average, the flux of $E > 100$ keV, $E > 300$ keV, and the count rate of $E > 1$ MeV trapped electrons peak 2, 2–4, and 5 days following storm onset, broadly consistent with previous estimates [e.g., *Li et al.*, 1997; *Rodger et al.*, 2010a]. The presence of these time delays is consistent with the gradual acceleration of a seed population of electrons to relativistic energies driven by enhanced whistler mode chorus waves [e.g., *Horne et al.*, 2005a], which are themselves associated with the periods of enhanced convection and repetitive substorm activity present during the passage of the high-speed solar wind stream.

[29] The global distribution as a function of L and MLT of the flux of precipitating $E > 30$ keV electrons during the passage of high-speed streams has a similar distribution to that observed during active conditions ($AE > 300$ nT) [*Lam et al.*, 2010]. The global morphology of the $E > 30$ keV electron precipitation during HSS-driven storms is also similar to the medium energy electron precipitation patterns during medium and high activity levels [*Codrescu et al.*, 1997]. The *Lam et al.* [2010] study showed that the global distribution of $E > 30$ keV electron precipitation is well correlated with the global distribution of lower band chorus waves observed by plasma wave experiment on the Combined Release and Radiation Effects Satellite(CRRES), suggesting that lower band chorus is very important for scattering $E > 30$ keV electrons from the Earth's inner magnetosphere into the atmosphere. However, this study was limited to $L < \sim 7$ due to the orbital coverage of the CRRES spacecraft. Here we extend our POES analysis out to $L = 9$ and note that at higher L ($7 < L < 9$) enhanced precipitation is seen in the prenoon sector that is largely absent in the postnoon sector and on the night side. Interestingly, recent wave observations from the THEMIS spacecraft show that, in the region $7 < L < 9$, chorus is also enhanced during disturbed conditions in the prenoon sector while being largely absent in the other sectors [*Li et al.*, 2009]. This is strong circumstantial evidence to suggest that chorus waves are also responsible for the precipitation of $E > 30$ keV electrons at higher L.

[30] There are a number of wave modes that could be responsible for the loss of relativistic electrons. Chorus waves resonate with electrons over a wide range of energies from a few hundred eV up to several MeV [e.g., *Horne et al.*, 2005a] and are a possible source of the MeV electron precipitation. Chorus waves are observed primarily outside the plasmapause on the dawnside [e.g., *Meredith et al.*, 2001; *Li et al.*, 2009] and are well correlated with the flux of precipitating $E > 30$ keV electrons [*Lam et al.*, 2010]. Our study shows that during the high-speed solar wind streams the bulk of the $E > 30$ keV electron precipitation occurs at $L > 5$ on the dawnside, inconsistent with the distribution of the freshly injected drift loss cone relativistic electrons, which peak inside L = 5 on the dayside (Figure 6, bottom). Plasmaspheric hiss and electromagnetic ion cyclotron waves also resonate with 1 MeV electrons, but the minimum resonant energies for scattering by EMIC waves are typically greater than 1 MeV inside $L = 5$ [*Meredith et al.*, 2003]. Furthermore, there is no well developed ring current to generate EMIC waves during HSS-driven storms. The pitch angle diffusion responsible for the relativistic electron precipitation is strongest in the region $3.5 < L < 5$ primarily on the dayside, extending from roughly 0500 MLT to 2100 MLT (Figure 6, bottom). This is consistent with the rates of pitch angle diffusion of radiation belt electrons during steady decay which are usually stronger on the dayside [*Selesnick et al.*, 2003] and the global distribution of plasmaspheric hiss which also tends to maximize on the dayside [*Meredith et al.*, 2004]. Our observations suggest that plasmaspheric hiss, which causes losses on a timescale of 5–6 days at $L = 4$ during quiet conditions [*Meredith et al.*, 2006], is most likely to be responsible for the bulk of the observed precipitation of MeV electrons before and during high-speed solar wind streams.

7. Conclusions

[31] We have performed a superposed epoch analysis of 42 HSS-driven storms using data from the NOAA POES spacecraft. Our principle conclusions are as follows:

[32] 1. The flux of trapped and precipitating $E > 30$ keV electrons increases immediately following storm onset and remains elevated during the passage of the high-speed solar wind stream.

[33] 2. The count rate of trapped and precipitating relativistic electrons, $E > 1$ MeV, drops out following storm onset over a wide range in L, and subsequently increase during the recovery phase to levels which eventually slightly exceed the prestorm levels.

[34] 3. There is no evidence for enhanced precipitation of relativistic electrons, $E > 1$ MeV, during the drop out of trapped relativistic electrons, suggesting that flux drop outs during the main phase of HSS-driven storms are not due to precipitation to the atmosphere.

[35] 4. During the passage of the high-speed stream, the flux of precipitating $E > 30$ keV electrons peaks in the region from 2100 to 1200 MLT at low L ($4 < L < 7$) and in the prenoon sector at high L ($7 < L < 9$), suggesting that chorus waves are responsible for the precipitation of $E > 30$ keV electrons in both regions.

[36] 5. The precipitating relativistic electron count rate peaks in the region near the SAA where both the bounce loss cone and equatorial pitch angle observed by the T0 telescope maximize. This could be caused by either an increase in the rate of pitch angle diffusion with equatorial pitch angle or larger fluxes of relativistic electrons at the edge of the bounce loss cone over the SAA.

[37] HSS-driven storms lead to increases in precipitation of energetic and relativistic electrons, leading to an almost continual supply of these particles during the declining phase of the solar cycle when these storms are most prevalent. Changes to atmospheric chemistry and, potentially surface level climate [*Seppälä et al.*, 2009], caused by energetic particle precipitation are likely to be most evident during the declining phase of the solar cycle.

[38] **Acknowledgments.** We thank the NSSDC Omniweb for providing the geomagnetic indices and solar wind parameters used in this study. This work was supported, in part, by the Natural Environment Research Council. J.E.B. and M.H.D. would like to thank all at BAS for their hospi-

tality during their visit in Spring 2010. Work at Lancaster was supported by STFC grant ST/G002401/1/.

[39] Robert Lysak thanks the reviewers for their assistance in evaluating this paper.

References

Baker, D. N., J. B. Blake, L. B. Callis, J. R. Cummings, D. Hovestadt, S. Kanekal, B. Klecker, R. A. Mewaldt, and R. D. Zwickl (1994), Relativistic electron acceleration and decay time scales in the inner and outer radiation belts: SAMPEX, *Geophys. Res. Lett.*, *21*, 409–412.

Baker, D. N., et al. (1997), Recurrent geomagnetic storms and relativistic electron enhancements in the outer magnetosphere: ISTP coordinated measurements, *J. Geophys. Res.*, *102*, 14,141–14,148.

Blake, J. B., D. N. Baker, N. Turner, K. W. Ogilvie, and R. P. Lepping (1997), Correlation of changes in the outer-zone relativistic electron population with upstream solar wind and magnetic field measurements, *Geophys. Res. Lett.*, *24*, 927–929.

Borovsky, J. E., and M. H. Denton (2008), A statistical look at plasmaspheric drainage plumes, *J. Geophys. Res.*, *113*, A09221, doi:10.1029/2007JA012994.

Borovsky, J. E., and M. H. Denton (2009a), Relativistic-electron dropouts and recovery: A superposed epoch study of the magnetosphere and the solar wind, *J. Geophys. Res.*, *114*, A02201, doi:10.1029/2008JA013128.

Borovsky, J. E., and M. H. Denton (2009b), Electron loss rates from the outer radiation belt caused by the filling of the outer plasmasphere: The calm before the storm, *J. Geophys. Res.*, *114*, A11203, doi:10.1029/2009JA014063.

Borovsky, J. E., and J. T. Steinberg (2006), The "calm before the storm" in CIR/magnetosphere interactions: Occurrence statistics, solar wind statistics, and magnetospheric preconditioning, *J. Geophys. Res.*, *111*, A07S10, doi:10.1029/2005JA011397.

Bortnik, J., R. M. Thorne, and N. P. Meredith (2008), The unexpected origin of plasmaspheric hiss from discrete chorus emissions, *Nature*, *452*, 62–66, doi:10.1038/nature06741.

Bortnik, J., R. M. Thorne, and N. P. Meredith (2009), Plasmaspheric hiss overview and relation to chorus, *J. Atmos. Sol. Terr. Phys.*, *71*, 1636–1646.

Burlaga, L. F., and R. P. Lepping (1977), The causes of recurrent geomagnetic storms, *Planet. Space Sci.*, *25*, 1151–1160.

Callis, L. B., D. N. Baker, M. Natarajan, J. B. Bernard, R. A. Mewaldt, R. S. Selesnick, and J. R. Cummings (1996), A 2-D model simulation of downward transport of NO_y into the stratosphere: Effects on the 1994 austral spring O_3 and NO_y, *Geophys. Res. Lett.*, *23*, 1905–1908.

Clilverd, M. A., A. Seppälä, C. J. Rodger, P. T. Verronen, and N. R. Thomson (2006), Ionospheric evidence of thermosphere-to-stratosphere descent of polar NO_x, *Geophys. Res. Lett.*, *33*, L19811, doi:10.1029/2006GL026727.

Clilverd, M. A., A. Seppälä, C. J. Rodger, N. R. Thomsen, J. Lichtenberger, and P. Steinbach (2007), Temporal variability of the descent of high altitude NO_x inferred from ionospheric data, *J. Geophys. Res.*, *112*, A09307, doi:10.1029/2006JA012085.

Clilverd, M. A., A. Seppälä, C. J. Rodger, M. G. Mlynczak, and J. U. Kozyra (2009), Additional stratospheric NO_x production by relativistic electron precipitation during the 2004 spring NO_x descent event, *J. Geophys. Res.*, *114*, A04305, doi:10.1029/2008JA013472.

Codrescu, M., T. Fuller-Rowell, R. Roble, and D. Evans (1997), Medium energy particle precipitation influences on the mesosphere and lower thermosphere, *J. Geophys. Res.*, *102*, 19,977–19,987.

Denton, M. H., and J. E. Borovsky (2008), Superposed epoch analysis of high-speed-stream effects at geosynchronous orbit: Hot plasma, cold plasma, and the solar wind, *J. Geophys. Res.*, *113*, A07216, doi:10.1029/2007JA012998.

Denton, M. H., and J. E. Borovsky (2009), The superdense plasma sheet in the magnetosphere during high-speed-stream driven storms: Plasma transport and timescales, *J. Atmos. Sol. Terr. Phys.*, *71*, 1045–1058, doi:10.1016/j.jastp.2008.04.023.

Denton, M. H., J. E. Borovsky, R. B. Horne, R. L. McPherron, S. K. Morley, and B. T. Tsurutani (2008), High-speed solar wind streams: A call for key research, *Eos Trans. AGU*, *89*(7), doi:10.1029/2008EO070002.

Denton, M. H., T. Ulich, and E. Turunen (2009), Modification of midlatitude ionospheric parameters in the F2 layer by persistent high-speed solar wind streams, *Space Weather*, *7*, S04006, doi:10.1029/2008SW000443.

Denton, M. H., J. E. Borovsky, and T. E. Cayton (2010), A density-temperature description of the outer radiation belt during geomagnetic storms, *J. Geophys. Res.*, *115*, A01208, doi:10.1029/2009JA014183.

Elphic, R. C., M. F. Thomsen, J. E. Borovsky, and D. J. McComas (1999), Inner edege of the electron plasma sheet: Empirical models of boundary location, *J. Geophys. Res.*, *104*, 22,679–22,693, doi:10.1029/1999JA900213.

Evans, D. S., and M. S. Greer (2004), Polar Orbiting Environmental Satellite Space Environment Monitor-2: Instrument descriptions and archive data documentation, *NOAA Tech. Mem. 93*, version 1.4, Space Weather Predict. Cent., Boulder, Colo.

Fraser, B. J., R. S. Grew, S. K. Morley, J. C. Green, H. J. Singer, T. M. Loto'aniu, and M. F. Thomsen (2010), Storm time observations of electromagnetic ion cyclotron waves at geosynchronous orbit: GOES results, *J. Geophys. Res.*, *115*, A05208, doi:10.1029/2009JA014516.

Gonzalez, W. D., B. T. Tsurutani, and A. L. Clua de Gonzalez (1999), Interplanetary origin of geomagnetic storms, *Space Sci. Rev.*, *88*, 529–562.

Grenfell, J. L., R. Lehmann, P. Mieth, U. Langematz, and B. Steil (2006), Chemical reaction pathways affecting stratospheric and mesospheric ozone, *J. Geophys. Res.*, *111*, D17311, doi:10.1029/2004JD005713.

Horne, R. B., and R. M. Thorne (1998), Potential waves for relativistic electron scattering and stochastic acceleration during magnetic storms, *Geophys. Res. Lett.*, *25*, 3011–3014.

Horne, R. B., R. M. Thorne, S. A. Glauert, J. M. Albert, N. P. Meredith, and R. R. Anderson (2005a), Timescale for radiation belt electron acceleration by whistler mode chorus waves, *J. Geophys. Res.*, *110*, A03225, doi:10.1029/2004JA010811.

Horne, R. B., et al. (2005b), Wave acceleration of electrons in the Van Allen radiation belts, *Nature*, *437*, 227–230, doi:10.1038/nature03939.

Horne, R. B., R. M. Thorne, S. A. Glauert, N. P. Meredith, D. Pokhotelov, and O. Santolik (2007), Electron acceleration in the Van Allen radiation belts by fast magnetosonic waves, *Geophys. Res. Lett.*, *34*, L17107, doi:10.1029/2007GL030267.

Horne, R. B., M. M. Lam, and J. C. Green (2009), Energetic electron precipitation from the outer radiation belt during geomagnetic storms, *Geophys. Res. Lett.*, *36*, L19104, doi:10.1029/2009GL040236.

Iles, R. H. A., A. N. Fazakerley, A. D. Johnstone, N. P. Meredith, and P. Bühler (2002),The relativistic electron response in the outer radiation belt during magnetic storms, *Ann. Geophys.*, *20*, 957–965.

Kennel, C., and H. Petschek (1966), Limit on stably trapped particle fluxes, *J. Geophys. Res.*, *71*, 1–28.

Kim, H.-J., and A. Chan (1997), Fully adiabatic changes in storm time relativistic electron fluxes, *J. Geophys. Res.*, *102*, 22,107–22,116.

Kozyra, J. U., et al. (2006), Response of the upper/middle atmosphere to coronal holes and powerful high-speed solar wind streams in 2003, in *Corotating Solar Wind Streams and Recurrent Geomagnetic Activity*, *Geophys. Monogr. Ser.*, vol. 167, edited by B. T. Tsurutani et al., pp. 319–340, AGU, Washington, D. C.

Lam, M. M., R. B. Horne, N. P. Meredith, and S. A. Glauert (2009), Radiation belt electron flux variability during three CIR-driven geomagnetic storms, *J. Atmos. Sol. Terr. Phys.*, *71*, 1145–1156.

Lam, M. M., R. B. Horne, N. P. Meredith, S. A. Glauert, T. Moffat-Griffin, and J. C. Green (2010), Origin of energetic electron precipitation >30 keV into the atmosphere, *J. Geophys. Res.*, *115*, A00F08, doi:10.1029/2009JA014619.

Lary, D. J. (1997), Catalytic destruction of stratospheric ozone, *J. Geophys. Res.*, *102*, 21,515–21,526.

Lauben, D. S., U. S. Inan, T. F. Bell, D. L. Kirchner, G. B. Hospodarsky, and J. S. Pickett (1998), VLF chorus emissions observed by Polar during the January 10, 1997, magnetic cloud, *Geophys. Res. Lett.*, *25*, 2995–2998.

Li, W., R. M. Thorne, V. Angelopoulos, J. Bortnik, C. M. Cully, B. Ni, O. LeContel, A. Roux, U. Auster, and W. Magnes (2009), Global distribution of whistler-mode chorus waves observed on the THEMIS spacecraft, *Geophys. Res. Lett.*, *36*, L09104, doi:10.1029/2009GL037595.

Li, X., D. N. Baker, M. Temerin, D. Larson, R. P. Lin, G. D. Reeves, M. Looper, S. G. Kanekal, and R. A. Mewaldt (1997), Are energetic electrons in the solar wind the source of the outer radiation belt?, *Geophys. Res. Lett.*, *24*, 923–926.

Li, X., D. N. Baker, S. G. Kanekal, M. Looper, and M. Temerin (2001), Long-term measurements of radiation belts by SAMPEX and their variations, *Geophys. Res. Lett.*, *28*, 3827–3830.

Lyons, L. R., D.-Y. Lee, H.-J. Kim, J. A. Hwang, R. M. Thorne, R. B. Horne, and A. J. Smith (2009), Solar-wind-magnetosphere coupling, including relativistic electron energization, during high-speed streams, *J. Atmos. Sol. Terr. Phys.*, *71*, 1059–1072, doi:10.1016/j.jastp.2008.04.016.

Madden, D., and M. S. Gussenhoven (1990), Auroral Boundary Index from 1983 to 1990, *Tech. Rep. GL-TR-90-0358*, Air Force Geophys. Lab., Hanscom AFB, Mass.

Meredith, N. P., R. B. Horne, and R. R. Anderson (2001), Substorm dependence of chorus amplitudes: Implications for the acceleration of electrons to relativistic energies, *J. Geophys. Res.*, *106*, 13,165–13,178.

Meredith, N. P., R. M. Thorne, R. B. Horne, D. Summers, B. J. Fraser, and R. R. Anderson (2003), Statistical analysis of relativistic electron energies for cyclotron resonance with EMIC waves observed on CRRES, *J. Geophys. Res.*, *108*(A6), 1250, doi:10.1029/2002JA009700.

Meredith, N. P., R. B. Horne, R. M. Thorne, D. Summers, and R. R. Anderson (2004), Substorm dependence of plasmaspheric hiss, *J. Geophys. Res.*, *109*, A06209, doi:10.1029/2004JA010387.

Meredith, N. P., R. B. Horne, S. A. Glauert, R. M. Thorne, D. Summers, J. M. Albert, and R. R. Anderson (2006), Energetic outer zone electron loss timescales during low geomagnetic activity, *J. Geophys. Res.*, *111*, A05212, doi:10.1029/2005JA011516.

Meredith, N. P., R. B. Horne, and R. R. Anderson (2008), Survey of magnetosonic waves and proton ring distributions in the Earth's inner magnetosphere, *J. Geophys. Res.*, *113*, A06213, doi:10.1029/2007JA012975.

Meredith, N. P., R. B. Horne, R. M. Thorne, and R. R. Anderson (2009), Survey of upper band chorus and ECH waves: Implications for the diffuse aurora, *J. Geophys. Res.*, *114*, A07218, doi:10.1029/2009JA014230.

Millan, R. M., and R. M. Thorne (2007), Review of radiation belt relativistic electron losses, *J. Atmos. Sol. Terr. Phys.*, *69*, 362–377, doi:10.1016/j.jastp.2006.06.019.

Miyoshi, Y., and R. Kataoka (2008), Flux enhancement of the outer radiation belt electrons after the arrival of stream interaction regions, *J. Geophys. Res.*, *113*, A03S09, doi:10.1029/2007JA012506.

Miyoshi, Y. S., V. K. Jordanova, A. Morioka, and D. S. Evans (2004), Solar cycle variations of the electron radiation belts: Observations and radial diffusion simulation, *Space Weather*, *2*, S10S02, doi:10.1029/2004SW000070.

Morley, S. K., R. H. W. Friedel, E. L. Spanswick, G. D. Reeves, J. T. Steinberg, J. Koller, T. Cayton, and E. Noveroske (2010a), Dropouts of the outer electron radiation belt in response to solar wind stream interfaces: Global positioning system observations, *Proc. R. Soc. A*, *466*, 3329–3350, doi:10.1098/rspa.2010.0078.

Morley, S. K., R. H. W. Friedel, T. E. Cayton, and E. Noveroske (2010b), A rapid, global and prolonged electron radiation belt dropout observed with the Global Positioning System constellation, *Geophys. Res. Lett.*, *37*, L06102, doi:10.1029/2010GL042772.

Nishimura, Y., et al. (2010), Identifying the driver of the pulsating aurora, *Science*, *330*, 81–84.

O'Brien, T. P., R. L. McPherron, D. Sornette, G. D. Reeves, R. Friedel, and H. J. Singer (2001), Which magnetic storms produce relativistic electrons at geosynchronous orbit?, *J. Geophys. Res.*, *106*, 15,533–15,544.

Paulikas, G. A., and J. B. Blake (1979), Effects of the solar wind on magnetospheric dynamics: Energetic electrons at synchronous orbit, in *Quantitative Modelling of Magnetospheric Processes*, *Geophys. Mongr. Ser.*, vol. 21, edited by W. P. Olsen, pp. 180–202, AGU, Washington, D. C.

Randall, C. E., et al. (2005), Stratospheric effects of energetic particle precipitation in 2003–2004, *Geophys. Res. Lett.*, *32*, L05802, doi:10.1029/2004GL022003.

Randall, C. E., V. L. Harvey, C. S. Singleton, P. F. Bernath, C. D. Boone, and J. U. Kozyra (2006), Enhanced NO_x in 2006 linked to strong upper stratospheric Arctic vortex, *Geophys. Res. Lett.*, *33*, L18811, doi:10.1029/2006GL027160.

Randel, W., et al. (2004), The SPARC intercomparison of middle-atmosphere climatologies, *J. Climate*, *17*, 986–1002.

Richardson, I. G., et al. (2006), Major geomagnetic storms ($Dst \leq -100$ nT) generated by corotating interaction regions, *J. Geophys. Res.*, *111*, A07S09, doi:10.1029/2005JA011476.

Rodger, C. J., M. A. Clilverd, J. C. Green, and M. M. Lam (2010a), Use of POES SEM-2 observations to examine radiation belt dynamics and energetic electron precipitation into the atmosphere, *J. Geophys. Res.*, *115*, A04202, doi:10.1029/2008JA014023.

Rodger, C. J., B. R. Carson, S. A. Cummer, R. J. Gamble, M. A. Clilverd, J. C. Green, J.-A. Sauvaud, M. Parrot, and J.-J. Berthelier (2010b), Contrasting the efficiency of radiation belt losses caused by ducted and nonducted whistler-mode waves from ground-based transmitters, *J. Geophys. Res.*, *115*, A12208, doi:10.1029/2010JA015880.

Rozanov, E., L. Callis, M. Schlesinger, F. Yang, N. Andronova, and V. Zubov (2005), Atmospheric response to NO_y due to energetic particle precipitation, *Geophys. Res. Lett.*, *32*, L14811, doi:10.1029/2005GL023041.

Sandanger, M. I., F. Soraas, M. Sorbo, K. Aarsnes, K. Oksavik, and D. S. Evans (2009), Relativistic electron losses related to EMIC waves during CIR and CME storms, *J. Atmos. Sol. Terr. Phys.*, *71*, 1126–1144, doi:10.1016/j.jastp.2008.07.006.

Scarf, F. L., R. W. Fredricks, C. F. Kennel, and F. V. Coroniti (1973), Satellite studies of magnetospheric substorms on August 15, 1968: 8. Ogo 5 plasma wave observations, *J. Geophys. Res.*, *78*, 3119–3130.

Selesnick, R. S. (2006), Source and loss rates of radiation belt relativistic electrons during magnetic storms, *J. Geophys. Res.*, *111*, A04210, doi:10.1029/2005JA011473.

Selesnick, R. S., J. B. Blake, and R. A. Mewaldt (2003), Atmospheric losses of radiation belt electrons, *J. Geophys. Res.*, *108*(A12), 1468, doi:10.1029/2003JA010160.

Seppälä, A., C. E. Randall, M. A. Clilverd, E. Rozanov, and C. J. Rodger (2009), Geomagnetic activity and polar surface air temperature variability, *J. Geophys. Res.*, *114*, A10312, doi:10.1029/2008JA014029.

Shprits, Y. Y. (2009), Potential waves for pitch-angle scattering of near-equatorially mirroring energetic electrons due to the violation of the second adiabatic invariant, *Geophys. Res. Lett.*, *36*, L12106, doi:10.1029/2009GL038322.

Shprits, Y. Y., R. M. Thorne, R. Friedel, G. D. Reeves, J. Fennell, D. N. Baker, and S. G. Kanekal (2006), Outward radial diffusion driven by losses at magnetopause, *J. Geophys. Res.*, *111*, A11214, doi:10.1029/2006JA011657.

Siskind, D. E., G. E. Nedoluha, C. E. Randall, M. Fromm, and J. M. Russell III (2000), An assessmant of southern hemisphere stratospheric NO_x enhancements due to transport from the upper atmosphere, *Geophys. Res. Lett.*, *27*, 329–332.

Smith, E. J., A. M. Frandsen, B. T. Tsurutani, R. M. Thorne, and K. W. Chan (1974), Plasmaspheric hiss intensity variations during magnetic storms, *J. Geophys. Res.*, *79*, 2507–2510.

St. Cyr, O., et al. (2000), Properties of coronal mass ejections: SOHO LASCO observations from January 1996 to June 1998, *J. Geophys. Res.*, *105*, 18,169–18,185.

Thomsen, M. F. (2004), Why Kp is such a good measure of magnetospheric convection, *Space Weather*, *2*, S11004, doi:10.1029/2004SW000089.

Thorne, R. M., E. J. Smith, K. J. Fiske, and S. R. Church (1974), Intensity variation of ELF hiss and chorus driving isolated substorms, *Geophys. Res. Lett.*, *1*, 193–196.

Thorne, R. M., S. R. Church, W. J. Malloy, and B. T. Tsurutani (1977), The local time variation of ELF emissions during periods of substorm activity, *J. Geophys. Res.*, *82*, 1585–1590.

Thorne, R. M., B. Ni, X. Tao, R. B. Horne, and N. P. Meredith (2010), Scattering by chorus waves as the dominant cause of diffuse auroral precipitation, *Nature*, *467*, 943–946, doi:10.1038/nature09467.

Tsurutani, B. T., and E. J. Smith (1974), Postmidnight chorus: A substorm phenomenon, *J. Geophys. Res.*, *79*, 118–127.

Tsurutani, B. T., and E. J. Smith (1977), Two types of magnetospheric ELGF chorus and their substorm dependencies, *J. Geophys. Res.*, *82*, 5112–5128.

Tsurutani, B. T., W. D. Gonzalez, A. L. C. Gonzalez, F. Tang, J. K. Arballo, and M. Okada (1995), Interplanetary origin of geomagnetic activity in the declining phase of the solar cycle, *J. Geophys. Res.*, *100*, 21,717–21,733.

Tu, W., R. Selesnick, X. Li, and M. Looper (2010), Quantification of the precipitation loss of radiation belt electrons observed by SAMPEX, *J. Geophys. Res.*, *115*, A07210, doi:10.1029/2009JA014949.

Turner, N. E., E. J. Mitchell, D. J. Knipp, and B. A. Emery (2006), Energetics of magnetic storms driven by corotating interation regions: A study of geoeffectiveness, in *Co-Rotating Solar Wind Streams and Recurrent Geomagnetic Activity*, *Geophys. Monogr. Ser.*, vol. 167, edited by B. T. Tsurutani et al., pp. 113–340, AGU, Washington, D. C.

Turunen, E., P. T. Verronen, A. Seppälä, C. J. Rodger, M. A. Clilverd, J. Tamminen, C.-F. Enell, and T. Ulich (2009), Impact of different energies of precipitating particles on NOx generation in the middle and upper atmosphere during geomagnetic storms, *J. Atmos. Sol. Terr. Phys.*, *71*, 1176–1189, doi:10.1016/j.jastp.2008.07.005.

J. E. Borovsky, Space Science and Applications, Los Alamos National Laboratory, Los Alamos, NM 87545, USA. (jborovsky@lanl.gov)

M. H. Denton, Department of Physics, Lancaster University, Lancaster LA1 4YW, UK. (m.denton@lancaster.ac.uk)

J. C. Green, Space Weather Prediction Center, National Oceanic and Atmospheric Administration, 325 Broadway Blvd., Boulder, CO 80305, USA. (janet.green@noaa.gov)

R. B. Horne and N. P. Meredith, British Antarctic Survey, Natural Environment Research Council, Madingley Road, Cambridge CB3 0ET, UK. (r.horne@bas.ac.uk; nmer@bas.ac.uk)

M. M. Lam, Department of Physics and Astronomy, University of Leicester, University Road, Leicester LE1 7RH, UK. (mml9@ion.le.ac.uk)